Materials Science & Engineering A 639 (2015) 37–41

Contents lists available at ScienceDirect

Materials Science & Engineering A

journal homepage: www.elsevier.com/locate/msea

Unusual behavior of the Portevin–Le Chatelier effect in an AlMg alloy containing precipitates

D.A. Zhemchuzhnikova [a,*], M.A. Lebyodkin [b], T.A. Lebedkina [b], R.O. Kaibyshev [a]

[a] Laboratory of Mechanical Properties of Nanoscale Materials and Superalloys, Belgorod State University, Pobeda 85, Belgorod 308015, Russia
[b] Laboratoire d'Etude des Microstructures et de Mécanique des Matériaux (LEM3), CNRS UMR 7239, Université de Lorraine, Ile du Saulcy, 57045 Metz, France

ARTICLE INFO

Article history:
Received 13 March 2015
Received in revised form
28 April 2015
Accepted 28 April 2015
Available online 8 May 2015

Keywords:
Aluminum alloys
Mechanical characterization
Precipitation
Plasticity
Deformation bands

ABSTRACT

Stress serration patterns and kinematics of deformation bands associated with the Portevin–Le Chatelier effect in an Al–Mg alloy were investigated by analyzing the evolution of the applied stress and axial strain distribution. In contrast to usually observed strain localization behaviors, referring to propagating and static deformation bands at high and low strain rates, respectively, the propagation mode was found to persist in a wide strain-rate range. This unusual behavior is discussed in relation with the role of precipitates.

1. Introduction

Due to their low weight and high mechanical strength, Al–Mg alloys are important technological materials for diverse applications in transportation industry [1,2]. However, their formability suffers from the phenomenon of plastic flow instability known as the Portevin–Le Chatelier (PLC) effect [1,3]. It characterizes mechanical behavior of various alloys and is generally attributed to dynamic strain aging (DSA), a mechanism caused by interaction between the mobile solute atoms and dislocations [4]. The instability occurs in some ranges of temperature, strain and strain rate, and results in strain localization in narrow bands leaving undesirable traces on the surface of the final product [5,6]. The abrupt plastic deformation within such bands gives rise to significant accelerations of the macroscopic strain rate, leading to stress drops on the stress–strain curves.

Binary Al–Mg alloys have been a model system for studying the PLC instability for a long time. The effects of various parameters, such as impurity concentration, grain size, dislocation structure, specimen and testing geometry, as well as external factors, e.g., application of electric current, were intensively investigated with regard to the proneness of the material to unstable deformation [7–11]. Furthermore, it was proven both experimentally [10,12–15] and theoretically [16–18] that the analysis of serration patterns and kinematic characteristics of the PLC bands can provide an important piece of information on the dynamical mechanisms responsible for the complexity of the behaviors observed. Three basic types of spatiotemporal behavior are usually distinguished when the strain rate or temperature are varied. Type *A* occurs at high enough strain rates. It is characterized by a repetitive propagation of deformation bands along the sample axis. The nucleation of a band, usually near one of the specimen ends, manifests itself as a rise in the stress and an abrupt fall back to or below the deformation curve (the so-called locking serrations). The subsequent smoother deformation corresponds to the band propagation towards the opposite end. At medium strain rates, this picture changes to a hopping propagation of localized bands. It gives rise to saw-like serrations, closely following each other, typically around the general level of the deformation curve (type *B*). Finally, this pattern is replaced with type *C* behavior upon further approaching the lower boundary of the strain-rate domain of instability. It is characterized by almost uncorrelated localized bands [19] resulting in deep stress drops below the deformation curve (unlocking serrations).

At the same time, the practical use of Al–Mg alloys is limited because of their low strength in annealed condition and strong susceptibility to stress-corrosion cracking in work-hardened condition, for Mg $\geq$3 wt% [1,2]. A substantial improvement of strength without loss in corrosion resistance and weldability could be reached by Sc and/or Zr additives due to the formation of Al_3(Sc, Zr) nanoscale precipitates [20]. However, their effect on the PLC instability is

* *Corresponding author. Tel./fax: +7 472 258 5456.
E-mail address: zhemchuzhnikova@bsu.edu.ru (D.A. Zhemchuzhnikova).

http://dx.doi.org/10.1016/j.msea.2015.04.094
0921-5093/

virtually unstudied. More generally, the influence of various precipitates on the PLC effect was mainly explored with regard to the conditions of its occurrence and the magnitude of stress drops [21,22]. Although the literature data testify that the secondary phase can also affect the serration patterns, this question mostly remained beyond the attention of researchers. The present paper dwells on the observation of a qualitative difference between spatiotemporal behavior of the investigated Al–Mg alloy containing precipitates and the above-described sequence of types associated with the PLC effect.

2. Experimental

The details of the alloy manufacturing procedure and the resulting microstructure were described elsewhere [23] and will be briefly outlined here. The alloy with the chemical composition Al–6%Mg–0.35%Mn–0.2%Sc–0.08%Zr–0.07%Cr (wt%) was produced by semi-continuous casting and homogenized for 12 h at 360 °C. The initial structure consisted of equiaxed grains with ~22 μm mean size and almost no sub-boundaries. The measurements of the dislocation density rendered values as low as 3×10^{12} m^{-2}. Two kinds of secondary phases were found within the grains: the major secondary phase consisting of uniformly distributed coherent Al_3(Sc,Zr) dispersoids with an average size about 10–15 nm, and sparse plate-like or round-shaped incoherent Al_6Mn dispersoids with an average thickness of 25 nm. In addition, some incoherent Al_3(Sc,Zr) particles 40 nm in size were detected on the grain boundaries. It was also found that interfaces between the coherent Al_3(Sc,Zr) dispersoids and the aluminum matrix exhibit high coherency strains [23].

Tensile specimens with a dog-bone shape and the gage section of $35 \times 7 \times 3$ mm^3 were machined from the ingot, mechanically polished with SiC papers up to 2400 grit, and tested at room temperature and constant grip velocity corresponding to the nominal applied strain rate, $\dot{\varepsilon}_a$, ranging from 3×10^{-5} s^{-1} to 4.3×10^{-2} s^{-1}. Two to four specimens were tested for each strain rate. Besides deformation curves, maps of the local strain rate versus time and position along the gage length were built using the technique described in [24]. It consists in recording the longitudinal displacements of a sequence of transversal surface markers, distant by 1 mm, with the aid of a CCD camera capturing their positions along the tensile axis of the specimen. The camera has a 20 mm field of vision, which allows for simultaneous recording of the positions of 20 markers, with a spatial resolution of 1.3 μm and a sampling frequency of 10^3 Hz. These data were then used to calculate values of the local strain and strain rate. In order to avoid any effect of the markers bending or inclination in the course of deformation, the camera was focused on the axis of symmetry of the specimen. Moreover, it was found that the markers remained perfectly normal to the tensile axis until failure (Fig. 1).

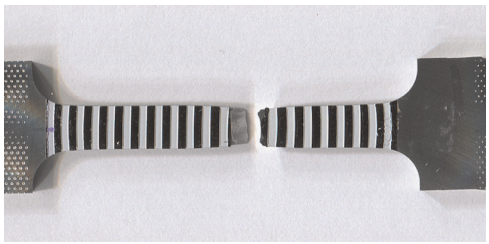

Fig. 1. Photograph of a specimen after failure. The apparent ridges at the borders of the white stripes are caused by an effect of contrast.

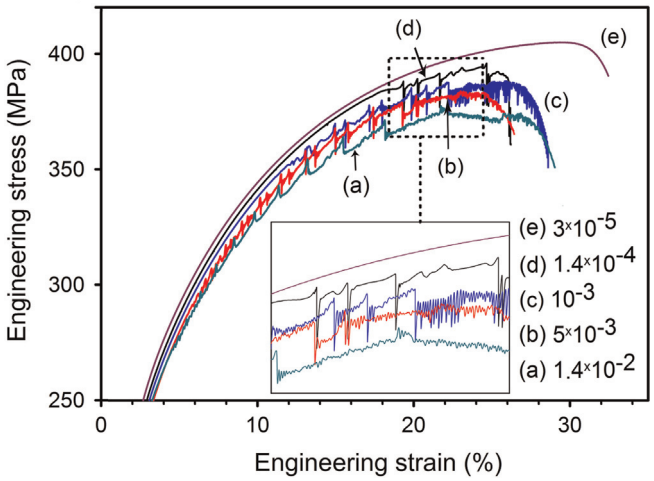

Fig. 2. Examples of deformation curves demonstrating different stress serration patterns. The values of the imposed strain rate are given in s^{-1} and placed against the respective deformation curve in the Inset. Curve (a) demonstrates type *A* behavior at a high strain rate, which becomes superposed with type *B* serrations at large strains; curves (b) and (c) correspond to mixed behaviors, with the dominating type *B*; curve (d) displays type *C* serrations at a low strain rate. The curves obtained at the highest strain rate of 4.3×10^{-2} s^{-1} were similar to the example (a).

3. Experimental results

Fig. 2 presents examples of stress–strain curves for several $\dot{\varepsilon}_a$ values. It can be seen that the curves recorded at higher $\dot{\varepsilon}_a$ systematically pass below those obtained at lower $\dot{\varepsilon}_a$ values, thus revealing negative strain-rate sensitivity, which is one of the basic predictions of the DSA theory. Accordingly, the PLC effect is observed for $\dot{\varepsilon}_a$ above 10^{-4} s^{-1} (curves *a*–*d*). It sets on after some critical strain ε_{cr} depending on $\dot{\varepsilon}_a$. The smooth deformation curve obtained at 3×10^{-5} s^{-1} (curve *e*) reflects the transition to stable plastic flow when $\dot{\varepsilon}_a$ is reduced below the boundary of the domain of plastic instability. The upper boundary was not attained even at the highest $\dot{\varepsilon}_a = 4.3 \times 10^{-2}$ s^{-1}.

The family of jerky curves presented in Fig. 2 displays the above-described features characteristic of the PLC effect but some peculiarities are also present, especially at low and intermediate strain rates. The repetitive stress humps observed at 1.4×10^{-2} s^{-1} (Fig. 2, curve *a*) and 4.3×10^{-2} s^{-1} correspond well to type *A* behavior. Similar to the literature data (e.g., [25]), a tendency to the development of type *B* oscillations between such stress humps is observed at large strain, although their amplitude remains small till rupture. This classification is confirmed by the corresponding strain-rate map shown in Fig. 3a. Indeed, a regular propagation of deformation bands through the entire field of vision of the CCD camera is found during the periods of a relatively smooth plastic flow separating the stress humps, whereas the end of the test is characterized by a competition between the continuous and hopping propagation, resulting in the propagation over shorter distances.

When the strain rate is decreased, the tendency to type *B* serrations and hopping propagation becomes stronger, as illustrated by curves *b* and *c* in Fig. 2 and their counterparts in Fig. 3. Indeed, compared to the above data for higher strain rates, the low-amplitude oscillations occur earlier (in strain) and develop in the course of the test; besides, the stress rises characteristic of the locking serrations are followed by relatively deep drops below the level of the deformation curve. This trend agrees with the *A*/*B* transition generally occurring when the strain rate is diminished. However, in contrast to the common observations, unmixed type *B* behavior was not found for the studied alloy, except for the late deformation stage at 10^{-3} s^{-1}: as illustrated by curve *c* in Fig. 2, regular type *B* serrations with large amplitudes only occur short

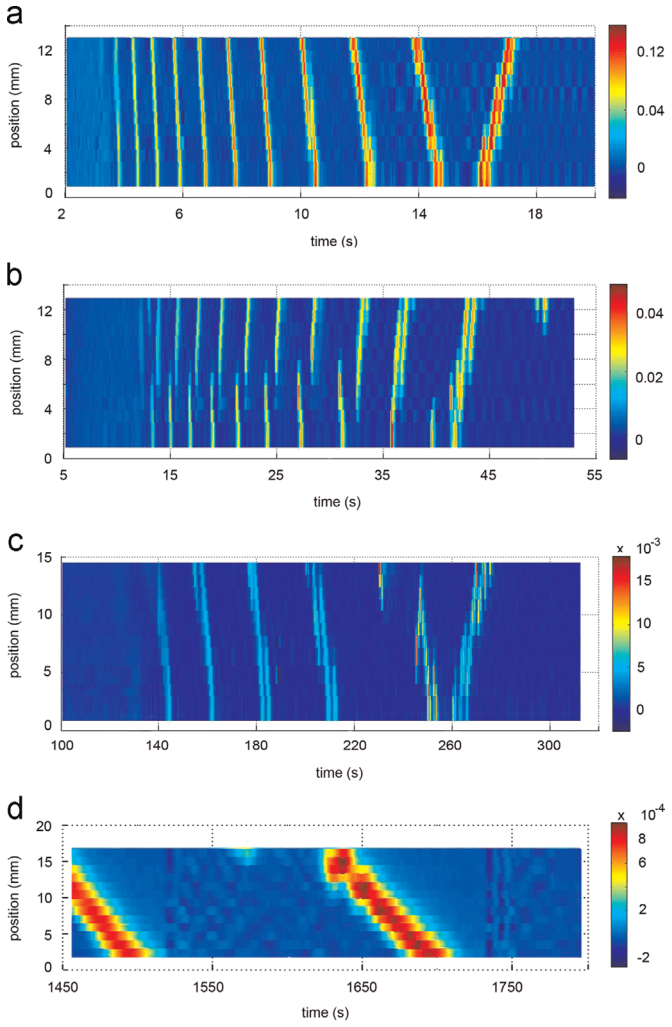

Fig. 3. Maps showing the time evolution of the local strain rate along the tensile axis. (a) $\dot{\varepsilon}_a = 1.4 \times 10^{-2}\,s^{-1}$; (b) $\dot{\varepsilon}_a = 5 \times 10^{-3}\,s^{-1}$; (c) $\dot{\varepsilon}_a = 10^{-3}\,s^{-1}$; and (d) $\dot{\varepsilon}_a = 1.4 \times 10^{-4}\,s^{-1}$. The color bars quantify the strain-rate scale (s^{-1}). (For interpretation of the references to color in this figure legend, the reader is referred to the web version of this article.)

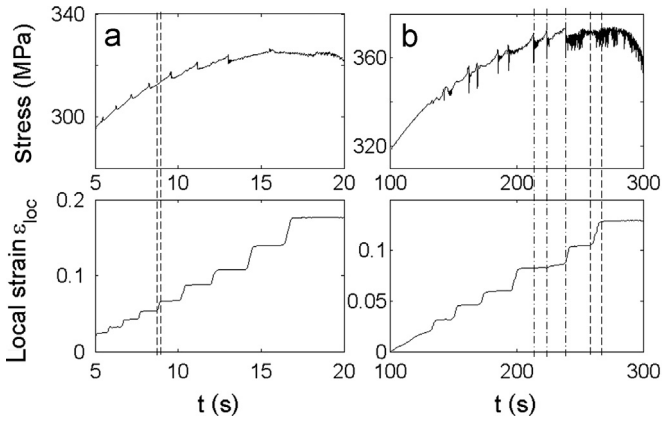

Fig. 4. Comparison of the deformation curve with the evolution of the local strain measured by one of the "extensometers" formed by the markers painted on the specimen surface. (a) $\dot{\varepsilon}_a = 1.4 \times 10^{-2}\,s^{-1}$and (b) $\dot{\varepsilon}_a = 10^{-3}\,s^{-1}$. The local strain was calculated relative to the "extensometer" length upon switching on the CCD camera. The dash-dotted lines point to several deep stress drops. The dashed lines show examples of strain steps that occur when the deformation bands pass the extensometer.

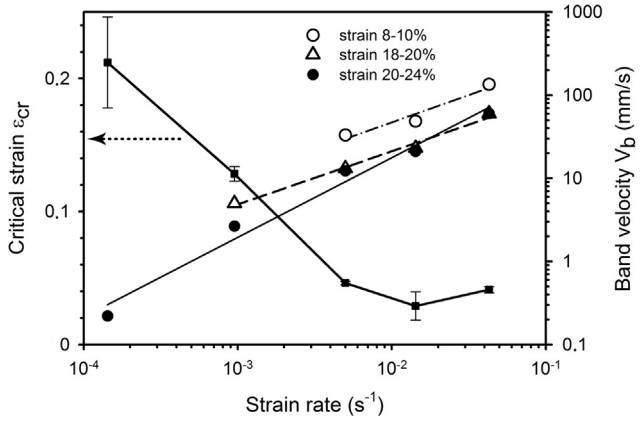

Fig. 5. Dependences of the band velocity V_b (circles and triangles) and critical strain ε_{cr} (squares) on the imposed strain rate. The standard error bars for ε_{cr} illustrate the data scatter between tests on different specimens. The mean values were not calculated for V_b because the deformation bands do not occur at the same strain values in different samples. The examples of V_b curves represent one series of tests. It was checked that other series render close results.

before the onset of necking; accordingly, the continuous traces of band propagation decay into a sequence of discrete deformation bands in Fig. 3c. Otherwise, type *A* behavior remains a primary mode, as it follows from the observation of both the characteristic features of stress serrations (Fig. 2, curves *b* and *c*) and long periods of virtually continuous propagation of deformation bands in Fig. 3b and c.

At $\dot{\varepsilon}_a = 1.4 \times 10^{-4}\,s^{-1}$ the deformation curves display easily recognizable type *C* serrations (Fig. 2d), in agreement with the closeness of this strain-rate value to the lower boundary of the domain of the PLC effect. Surprisingly, instead of randomly occurring static deformation bands characteristic of type *C* behavior, a perfect propagation of deformation bands with a velocity V_b as low as 0.2 mm/s is detected for this strain rate, as presented in Fig. 3d. It is also noteworthy that the observed stress serrations keep some tendency to display stress rises before the subsequent deep stress drops.

An additional proof of the persistent character of the propagation behavior is provided by the curves of evolution of the local strain measured by one of the painted "extensometers", as illustrated in Fig. 4 for a high (a) and intermediate (b) strain rate. Fig. 4(a) presents a typical dependence of the local strain rate observed when deformation bands are nucleated close to one specimen end and propagate to the other end, so that the local strain rapidly increases only during short periods when the deformation bands pass the corresponding extensometer (cf. [26]). Similar patterns were observed at the lowest strain rate. Fig. 4(b) clarifies the peculiarities related to the concurrency between the continuous and hopping propagation at an intermediate strain rate. The dash-dotted lines project the instants of deep stress drops onto the local strain curve and present examples of the extensometer reaction when the deformation band is nucleated either outside or within the extensometer width. A fast strain increment is observed in the latter case. Some spring back effects can also be recognized as low-amplitude strain drops. The dashed lines delimit a strain step during neat type *B* serrations observed at large strains. It is composed of three steps reflecting the propagation of three deformation bands visualized in Fig. 3(c). It can be supposed that the sites of nucleation of the deformation bands corresponding to sequential stress serrations are correlated so strongly that the hopping and continuous propagation become indistinguishable.

In order to verify whether the propagation behavior is the same over the whole $\dot{\varepsilon}_a$ range, Fig. 5 presents the effects of $\dot{\varepsilon}_a$ and ε on V_b. The overall dependence was only obtained for large strain (solid

circles) because ε_{cr} exceeds 0.2 at $\dot{\varepsilon}_a = 1.4 \times 10^{-4}\,s^{-1}$, as illustrated in the same figure (squares). It can be seen that each dataset corresponding to a similar strain interval obeys a unique dependence on $\dot{\varepsilon}_a$, thus testifying that the same mechanism governs the dynamics of deformation bands all over the strain-rate range. The entirety of results qualitatively agrees with the literature data which either correspond to type *A* regime or combine measurements for the continuous (type *A*) and hopping (type *B*) propagation. Namely, V_b decreases with strain hardening, such slowing down being generally ascribed to the increasing number of obstacles to the dislocation motion; its strain-rate dependence obeys a power law $V_b \propto \dot{\varepsilon}_a^{\alpha}$, with α tending to increase with strain (cf. [26,27]). The data of Fig. 5 allow for an accurate estimation of the maximum α corresponding to a strain interval $0.2 < \varepsilon < 0.24$, $\alpha = 0.96 \pm 0.08$, which agrees with the maximum α found in [27] for an Al–3%Mg alloy.

An additional verification stems from the evaluation of the local strain rate within a deformation band. Such estimates render values exceeding $\dot{\varepsilon}_a$ by an order of magnitude (cf. color bars in Fig. 3). This ratio is consistent with the literature data for type *A* deformation bands. In contrast, it is two orders of magnitude smaller than that reported for type *B* bands [26]. It can thus be concluded that the propagation features observed for the investigated alloy over the entire $\dot{\varepsilon}_a$ range are conform to those expected for type *A* behavior.

4. Discussion and concluding remarks

To our knowledge, such a persistence of the band propagation mode has not been observed nor predicted for the PLC effect so far. Moreover, the existing models handling the dynamics of the PLC effect tend to reproduce the transitions between the three types of serration patterns and deformation band kinematics [16–18].

A hint to understanding this peculiarity can be found in its striking similarity with the persistent propagation of deformation bands in twinning induced plasticity (TWIP) steels, the deformation of which is governed by a combination of dislocation glide and twinning [24]. Although the unstable plastic flow in TWIP steels is usually attributed to the PLC effect, such persistent band propagation has not been explained so far. It is known that Al–Mg alloy are not prone to mechanical twinning. More specifically, the absence of twins in the investigated alloy was proven in [23]. Therefore, the similarity of the kinematics of deformation bands in two materials cannot be ascribed to a unique microstructure feature, such as twinning. A common property of these materials is that both twin boundaries and precipitates are efficient obstacles to dislocation motion, which locally harden the material and generate internal stresses promoting plastic flow in the neighboring areas. It can thus be suggested in context of [24] that the mechanism of strain propagation in the present alloy is due to overstresses originating from the coherent Al_3(Sc,Zr) dispersoids.

The presence of such uniformly distributed precipitates is also likely to distinguish the studied case from the investigations of the deformation band kinematics reported in the literature. Such investigations were mostly performed on binary or commercially pure Al–Mg or Al–Cu alloys and revealed the well-known transition from deformation band propagation to static bands (e.g., [12,14,15,27]). Although their chemical composition and microstructure are often insufficiently specified, the available data allow for a conclusion that the presence of many impurities, e.g., Mn and Cr, also present in the investigated alloy, do not modify the usual band kinematics. Therefore, the above hypothesis should be discussed in more detail.

Indeed, it is corroborated by several observations bearing witness to an important role of precipitates in the investigated alloy. To begin with, compared to the binary Al–Mg alloys displaying jerky flow approximately in the $\dot{\varepsilon}_a$ range from $10^{-6}\,s^{-1}$ to $10^{-2}\,s^{-1}$, the domain of instability illustrated in Fig. 2 is significantly shifted to the range of high strain rates. This shift can be easily understood in the framework of the DSA mechanism. Indeed, the DSA model is based on the consideration of interplay between the characteristic diffusion time of solute atoms, t_d, and the waiting time t_w that a dislocation spends arrested on obstacles and waiting for thermal activation [4]. Forest dislocations are considered as the main obstacles to the motion of dislocations in dilute single-phase alloys. The solute atoms diffuse to the dislocation during t_w and additionally pin it. The deformation is stable in two limiting cases. First, when $\dot{\varepsilon}_a$ is high enough ($t_w \ll t_d$), the dislocations are unaffected by solutes. Second, when $\dot{\varepsilon}_a$ is low ($t_w \gg t_d$), the solute atoms form a saturated cloud moving together with the dislocation. In contrast to these cases, when t_w and t_d are comparable, the motion of a dislocation can be seen as pinning–unpinning events. As the stress required to unpin the dislocation from solutes is higher than for its solute-free motion, the behavior becomes unstable and leads to jumps in the strain rate. This picture helps understanding the shift of the domain of instability to the range of higher $\dot{\varepsilon}_a$ values for a material with precipitates, as a result of an increase in the number and, perhaps, strength of obstacles to the motion of dislocations and, consequently, an increase in the average waiting time.

Furthermore, Fig. 5 reveals that ε_{cr} decreases with increasing $\dot{\varepsilon}_a$ in a large interval, thus following the so-called “inverse” dependence on the strain rate. The nature of such behavior remains a matter of debate up to now [28]. The early models based on the DSA mechanism and considering the evolution of the densities of mobile and forest dislocations during deformation predicted an increase in ε_{cr} with increasing $\dot{\varepsilon}_a$ (“normal” behavior) [4]. However, “inverse” behavior was often observed at low strain rates [8,21,28,29]. Recent modifications of the DSA model, which suggest a strain dependence of the DSA contribution to the work hardening, could also be applied for interpretation of such a nonmonotonous dependence [30,31]. However, it has been noticed very early that precipitates can render an alternative mechanism for inverse behavior [21]. This hypothesis received a direct confirmation in [8], where a change from normal to inverse behavior was realized by increasing the Mg concentration and favoring the precipitation. The modification of the DSA model due to precipitates was theoretically treated in [32]. The analysis of a concurrency between the deformation-induced dissolution of precipitates and the nucleation of new ones led to a conclusion that small precipitates shearable by dislocations, such as coherent Al_3(Sc,Zr) particles with size $\sim$10 nm [33], can give rise to a nonmonotonous strain-rate dependence of ε_{cr}. Therefore, the observation of inverse behavior in the studied material is consistent with these predictions.

In summary, the PLC effect was investigated at room temperature in an Al–Mg alloy containing nanoscale coherent precipitates. It was found that when the applied strain rate is varied, the serration patterns display features which can be recognized according to the known types of behavior referred to as types *A*, *B*, and *C*. These types of serrations are usually associated with the transitions from a continuous propagation of deformation bands to a hopping propagation and finally to the occurrence of static bands. Nevertheless, the propagation mode was found to persist in the investigated alloy over the entire strain-rate range. This unusual behavior was attributed to the role of precipitates as sites where the dislocation piling-up increases the internal stress level and favors the strain propagation. It is noteworthy that such behavior is not predicted by the current PLC models and opens new prospective for a better understanding of plastic instability in complex alloys.

Acknowledgments

The authors are grateful to P. Moll for help in experiments. D. Zh. acknowledges support by the Ministry of Education and Science, Russia, (Belgorod State University, Grant no. 1533) and the Research Federation GI2M (Metz, France) for her stays in Metz in 2014. T.L. acknowledges support by the Center of Excellence "LabEx DAMAS" (Grant ANR-11-LABX-0008-01 of the French National Research Agency).

References

[1] I.J. Polmear, Light Alloys: From Traditional Alloys to Nanocrystals, fourth ed., Butterworth-Heinemann/Elsevier, UK, 2006.
[2] E.M. Taleff, P.J. Nevland, E. Krajewski, Metall. Mater. Trans. A 32A (2001) 1119–1130.
[3] A. Portevin, F. Le Chatelier, C. R. Acad. Sci. Paris 176 (1923) 507–510.
[4] Y. Estrin, L.P. Kubin, J. Mech. Behav. Metals 2 (1990) 255–292.
[5] H. Halim, D.S. Wilkinson, M. Niewczas, Acta Mater. 55 (2007) 4151–4160.
[6] E. Samuel, J.J. Jonas, F.H. Samuel, Metall. Mater. Trans. A 42F (2011) 1028–1037.
[7] M. Wagenhofer, M.A. Erickson-Natishan, R.W. Armstrong, F.J. Zerilli, Scr. Mater. 41 (1999) 1177–1184.
[8] K. Chihab, H.H. Ait-Amokhtar, K. Bouabdellan, Ann. Chim. Sci. Mater. 27 (2002) 69–75.
[9] J. Zdunek, W.L. Spychalski, J. Mizera, K.J. Kurzydowski, Mater. Charact. 58 (2007) 46–50.
[10] T.A. Lebedkina, M.A. Lebyodkin, Acta Mater. 56 (2008) 5567–5574.
[11] L. Ziani, S. Boudrahem, H. Ait-Amokhtar, et al., Mater. Sci. Eng. A 536 (2012) 239–243.
[12] K. Chihab, Y. Estrin, L.P. Kubin, J. Vergnol, Scr. Metall. 21 (1987) 203–208.
[13] M.S. Bharathi, M. Lebyodkin, G. Ananthakrishna, et al., Phys. Rev. Lett. 87 (2001) 165508/1–165508/4.
[14] H. Louche, P. Vacher, R. Arrieux, Mater. Sci. Eng. A 404 (2005) 188–196.
[15] Q. Zhang, Z. Jiang, H. Jiang, et al., Int. J. Plast. 21 (2005) 2150–2173.
[16] S. Kok, M.S. Bharathi, A.J. Beaudoin, et al., Acta Mater. 51 (2003) 3651–3662.
[17] E. Rizzi, P. Hähner, J. Int. Plast. 20 (2004) 121–165.
[18] J. Kumar, G. Ananthakrishna, Phys. Rev. Lett. 106 (2011) 106001.
[19] M.A. Lebyodkin, T.A. Lebedkina, Phys. Rev. E 77 (2008) 026111.
[20] Yu.A. Filatov, V.I. Yelagin, V.V. Zakharov, Mater. Sci. Eng. A 280 (2000) 97–101.
[21] P.G. McCormick, Scr. Metall. 6 (1972) 165–170.
[22] S. Kumar, H.B. McShane, Scr. Metall. Mater. 28 (1993) 1149–1154.
[23] D. Zhemchuzhnikova, A. Mogucheva, R. Kaibyshev, Mater. Sci. Eng. A 565 (2013) 132–141.
[24] T.A. Lebedkina, M.A. Lebyodkin, J.-Ph. Château, et al., Mater. Sci. Eng. A 519 (2009) 147–154.
[25] I.V. Shashkov, M.A. Lebyodkin, T.A. Lebedkina, Acta Mater. 60 (2012) 6842–6850.
[26] H. Ait-Amokhtar, P. Vacher, S. Boudrahem, Acta Mater. 54 (2006) 4365–4371.
[27] F.B. Klose, F. Hagemann, P. Hähner, H. Neuhäuser, Mater. Sci. Eng. A 387–389 (2004) 93–97.
[28] J. Balík, P. Lukáč, L.P. Kubin, Scr. Mater. 42 (2000) 465–471.
[29] S. Kumar, Scr. Metall. Mater. 33 (1995) 81–86.
[30] T. Böhlke, G. Bondár, Y. Estrin, M.A. Lebyodkin, Comput. Mater. Sci. 44 (2009) 1076–1088.
[31] M. Mazière, H. Dierke, Comput. Mater. Sci. 52 (2012) 68–72.
[32] Y. Brechet, Y. Estrin, Acta Metall. Mater. 43 (1995) 955–963.
[33] F. Fazeli, W.J. Poole, C.W. Sinclair, Acta Mater. 56 (2008) 1909–1918.